A three-dimensional high-order generalized FEM for through-the-thickness branched cracks*

C. A. Duarte[a,1], L. G. Reno[a], A. Simone[b]

[a] *Department of Civil and Environmental Engineering, University of Illinois at Urbana-Champaign*
2122 Newmark Laboratory MC 250, 205 North Mathews Av., Urbana, Illinois 61801, USA

[b] *Faculty of Civil Engineering and Geosciences, Delft University of Technology*
P.O. Box 5048, 2600 GA, Delft, The Netherlands

SUMMARY

This paper presents high-order implementations of a generalized finite element method for through-the-thickness three-dimensional branched cracks. This approach can accurately represent discontinuities such as triple joints in polycrystalline materials and branched cracks, independently of the background finite element mesh. Representative problems are investigated to illustrate the accuracy of the method in combination with various discretizations and refinement strategies. The combination of local refinement at crack fronts and high-order continuous and discontinuous enrichments proves to be an excellent combination which can deliver convergence rates close to that of problems with smooth solutions.

KEY WORDS: branched crack; generalized finite element method; *hp*-method; high-order finite elements; partition of unity; x-fem

1. INTRODUCTION

Crack branching is a distinctive feature of many failure mechanisms. Problems as diverse as corrosion assisted cracking [1, 2] and high velocity impact or dynamic crack propagation [3–5] are characterized by the appearance of branched cracks. In this paper, we present extensions of the GFEM presented in [6] that are able to handle through-the-thickness three-dimensional branched discontinuities which are independent of the finite element mesh. The combination of mesh independent discontinuities and of the proposed high-order GFEM approximations provides a very flexible and robust method that can deliver accurate solutions and high convergence rates.

The finite element analysis of crack branching problems poses challenging demands already at the discretization stage. The singularities at crack fronts require strongly refined meshes that must fit the discontinuity surfaces while keeping the aspect ratio of the elements within acceptable bounds [7–14]. These requirements are not always met or may be satisfied by using a large number of elements. Meshing around the branching surface can also be difficult and leads to a large number of elements when the angle between the branches is small.

[1] Correspondence to: C. A. Duarte (caduarte@uiuc.edu)

* Submitted to *International Journal for Numerical Methods in Engineering*: Submitted on September 22, 2006.

Algorithms such as Delaunay triangulation are heavily applied to generate unstructured meshes [11, 15]. These algorithms maximize the minimum angle in the mesh with the intent of producing a mesh with equilateral triangles. Unfortunately, complex geometries may cause the generation of an enormous quantity of elements to satisfy mesh quality constraints at the expenses of increased computational cost. Another drawback of many Delaunay-based meshing methods is the appearance of sliver elements in three-dimensional domains [9, 10]. These elements have a detrimental effect on the accuracy of the finite element solution. Their removal is usually done through a mesh optimization step which adds to the mesh generation time and requires a certain amount of user intervention.

The work presented in this paper builds upon the generalized FEM for polycrystals recently proposed by Simone et al. [6]. Here, the displacement field is enriched with high-order hierarchical GFEM approximations. These hierarchical approximations are built to account for the discontinuous nature of the displacement field across crack surfaces with a procedure similar to that devised in [16–18] for a continuous field alone. Our GFEM shape functions are however equivalent to those proposed by Daux et al. [19] in the case of piece-wise linear approximations in two-dimensions. This equivalence is discussed in details in [6]. In the case of a single (non-branching) discontinuity and piece-wise linear approximations, the proposed GFEM shape functions reduce to those proposed in [20]. Theoretical aspects of our approach are illustrated in Section 2.

At variance with the established enrichment of the displacement field with discontinuous functions and the use of linear approximations proposed by Moës et al. [20] in the so-called X-FEM, approximation orders higher than one have been exploited in various forms by Wells and Sluys [21], Stazi et al. [22], Chessa et al. [23], Mariani and Perego [24], and Laborde et al. [25]. In this work, we have consistently used high-order hierarchical GFEM approximations for single and multi-branched cracks. High-order enrichment functions are used with a linear finite element partition of unity. Therefore, all nodal degrees of freedom are defined at element vertex nodes which facilitates mesh generation, specially in three-dimensional computations. This is in contrast with the use of high-order non-hierarchical Lagrangian partition of unity functions with piece-wise constant enrichment functions [21–23, 25]. This approach leads to nodes on element edges, faces and interior. Hierarchical approximations are also ideal for the construction of non-uniform polynomial approximations which can be very effective for some class of problems [26]. Other advantages of hierarchical GFEM, such as the non-zero structure of the resulting stiffness and mass matrices, are discussed in [16–18]. The issue of linear dependence of hierarchical GFEM enrichments is also discussed in details in [18].

The combination of the proposed high-order GFEM approximations with non-uniform meshes is discussed in Section 3. There, we show the results obtained in a convergence study using this type of discretization for problems with through-the-thickness single and branched cracks. A comparison of various discretizations and refinement strategies reported in Section 3.1 shows that the use of *p*-enrichment on locally refined mesh is the most efficient strategy to achieve accurate solutions and high convergence rates, even without the use of crack front enrichment functions [25, 27]. This specific choice has the advantage of preserving a conforming approximation without the necessity to enrich several layers of elements around the crack front, as otherwise proposed by Laborde et al. [25]. Further, it enhances the flexibility of the approach as crack front enrichment functions, when known, are difficult to integrate.

2. HIGH-ORDER APPROXIMATIONS FOR BRANCHED CRACKS

Branched cracks in two- and three-dimensions can be described with the GFEM for polycrystalline structures presented in [6]. Here, we adapt that formulation to the case of branched cracks and improve it using high-order enrichment functions. The formulation is valid for branched cracks with arbitrary number of branches. However, the illustration of the main ideas is done with the aid of the two-dimensional case shown in Figure 1. We also assume that crack fronts are located at the boundary of elements. This approach was originally proposed in [21] and greatly simplifies the computational implementation. Introductory references on the generalized FEM are, e.g., in [17, 18, 28, 29]. In this section, we assume the reader has some basic understanding of the method.

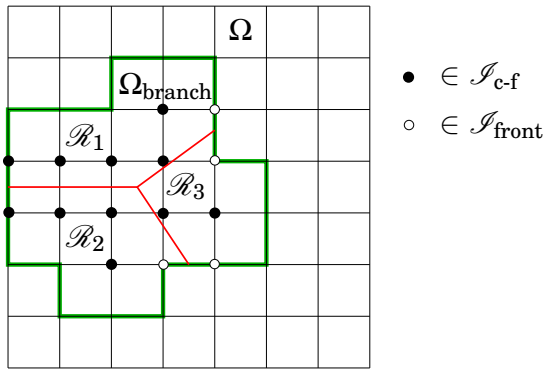

Figure 1. Neighborhood of a branched crack in a two-dimensional domain.

Consider a domain Ω with a branched crack as illustrated in Figure 1. This domain may, in turn, be a subdomain of a larger domain with several branched cracks. Let $\mathscr{I}_{\text{front}}$ denote a set with the indices of nodes/finite element partition of unity functions, φ_α, whose supports, ω_α, intersect a crack front. Note that since a finite element is an open set, the intersection of an element with a crack front located at its boundary is empty. Let $\mathscr{I}_{\text{crack}}$ denote the indices of nodes/finite element partition of unity functions whose supports intersect a crack surface. The set $\mathscr{I}_{\text{c-f}}$ contains the indices that belong to $\mathscr{I}_{\text{crack}}$ but not to $\mathscr{I}_{\text{front}}$, i.e., $\mathscr{I}_{\text{c-f}} = \mathscr{I}_{\text{crack}} - \mathscr{I}_{\text{front}}$.

A neighborhood of a branched crack is a domain defined by

$$\Omega_{\text{branch}} = \bigcup_{\alpha \in \mathscr{I}_{\text{c-f}}} \omega_\alpha \tag{1}$$

The crack surfaces divide Ω_{branch} in $N_{\mathscr{R}}$ non-overlapping regions denoted by $\mathscr{R}_i$, $i = 1, \ldots, N_{\mathscr{R}}$, i.e.,

$$\bar{\Omega}_{\text{branch}} = \bigcup_{i=1}^{N_{\mathscr{R}}} \bar{\mathscr{R}}_i, \qquad \mathscr{R}_i \cap \mathscr{R}_j = \emptyset \quad \text{if } i \neq j \tag{2}$$

In the case of the triple joint shown in Figure 1, for example, Ω_{branch} is divided in three regions. The derivation of GFEM approximations defined in Ω_{branch} is analogous to that used for polycrystalline structures presented in [6].

The elasticity solution $\boldsymbol{u}$ in Ω_{branch} is of the form

$$\boldsymbol{u} = \hat{\boldsymbol{u}} + \sum_{i=1}^{N_{\mathscr{R}}} \mathscr{H}_i \tilde{\boldsymbol{u}}_i, \tag{3}$$

where $\mathscr{H}_i(\boldsymbol{x})$ denotes a discontinuous function defined by

$$\mathscr{H}_i(\boldsymbol{x}) = \begin{cases} 1 & \text{if } \boldsymbol{x} \in \mathscr{R}_i \\ 0 & \text{otherwise} \end{cases}, \tag{4}$$

while $\hat{\boldsymbol{u}}$ and $\tilde{\boldsymbol{u}}_i,\ i = 1,\ldots,N_{\mathscr{R}}$, are continuous functions defined on Ω_{branch} and $\mathscr{R}_i$, respectively. We assume that the crack surfaces are not in contact. In the case of contact, the non-penetration of crack surfaces can be enforced using, for example, a cohesive formulation with a very stiff cohesive stiffness in the direction normal to the surfaces. The procedure is analogous to that used in [6] to avoid penetration of grain boundaries in a polycrystalline structure.

A partition of unity approximation of polynomial degree p, $\hat{\boldsymbol{u}}^{hp}$, of $\hat{\boldsymbol{u}}$ is given by

$$\hat{\boldsymbol{u}}^{hp} = \sum_{\alpha=1}^{N_b} \varphi_\alpha(\boldsymbol{x})\hat{\boldsymbol{u}}_\alpha^{hp}(\boldsymbol{x}) = \sum_{\alpha=1}^{N_b} \varphi_\alpha(\boldsymbol{x}) \sum_{j=1}^{D_L} \underline{\hat{\boldsymbol{u}}}_{\alpha j} L_{j\alpha}(\boldsymbol{x}) = \sum_{\alpha=1}^{N_b}\sum_{j=1}^{D_L} \underline{\hat{\boldsymbol{u}}}_{\alpha j}\hat{\phi}_{j\alpha}(\boldsymbol{x}) \tag{5}$$

where N_b is the number of nodes in the mesh defining Ω_{branch}, $\hat{\boldsymbol{u}}_\alpha^{hp},\ \alpha = 1,\ldots,N_b$, are local approximations of $\hat{\boldsymbol{u}}$ defined on ω_α, $\underline{\hat{\boldsymbol{u}}}_{\alpha j}$ and $\hat{\phi}_{j\alpha}(\boldsymbol{x}) = \varphi_\alpha(\boldsymbol{x})L_{j\alpha}(\boldsymbol{x}),\ \alpha = 1,\ldots,N_b,\ j = 1,\ldots,D_L$ are nodal degrees of freedom and generalized finite element shape functions of degree p, respectively, and D_L is the dimension of a set of polynomial enrichment functions of degree less or equal to $p-1$. Our implementation follows [17, 18] and the set $\{L_{j\alpha}\}_{j=1}^{D_L}$ for a node $\boldsymbol{x}_\alpha = (x_\alpha, y_\alpha, z_\alpha)$ is given by

$$\{L_{j\alpha}\}_{j=1}^{D_L} = \left\{1, \frac{(x-x_\alpha)}{h_\alpha}, \frac{(y-y_\alpha)}{h_\alpha}, \frac{(z-z_\alpha)}{h_\alpha}, \frac{(x-x_\alpha)^2}{h_\alpha^2}, \frac{(y-y_\alpha)^2}{h_\alpha^2}, \ldots\right\}$$

with h_α being a scaling factor [17, 18]. These enrichment functions and the corresponding generalized FE shape functions, $\hat{\phi}_{j\alpha}$, are identical to those defined in [18] for tetrahedral elements.

Partition of unity approximations of degree p for $\tilde{\boldsymbol{u}}_i,\ i = 1,\ldots,N_{\mathscr{R}}$, are given by

$$\tilde{\boldsymbol{u}}_i^{hp} = \sum_{\alpha=1}^{N_b} \varphi_\alpha(\boldsymbol{x})\tilde{\boldsymbol{u}}_{i\alpha}^{hp}(\boldsymbol{x}) = \sum_{\alpha=1}^{N_b} \varphi_\alpha(\boldsymbol{x}) \sum_{j=1}^{D_L} \underline{\tilde{\boldsymbol{u}}}_{i\alpha j} L_{j\alpha}(\boldsymbol{x}) \tag{6}$$

where $\tilde{\boldsymbol{u}}_{i\alpha}^{hp},\ \alpha = 1,\ldots,N_b$, are local approximations of $\tilde{\boldsymbol{u}}_i$ defined on ω_α and $\underline{\tilde{\boldsymbol{u}}}_{i\alpha j},\ \alpha = 1,\ldots,N_b,\ j = 1,\ldots,D_L$, are nodal degrees of freedom.

From the above, we have that a partition of unity approximation, $\boldsymbol{u}^{hp}$, of $\boldsymbol{u}$ is given by

$$\begin{aligned}
\boldsymbol{u}^{hp}(\boldsymbol{x}) &= \sum_{\alpha=1}^{N_b} \varphi_\alpha(\boldsymbol{x})\hat{\boldsymbol{u}}_\alpha^{hp}(\boldsymbol{x}) + \sum_{i=1}^{N_{\mathscr{R}}} \mathscr{H}_i(\boldsymbol{x}) \sum_{\alpha=1}^{N_b} \varphi_\alpha(\boldsymbol{x})\tilde{\boldsymbol{u}}_{i\alpha}^{hp}(\boldsymbol{x}) \\
&= \sum_{\alpha=1}^{N_b} \varphi_\alpha(\boldsymbol{x}) \left[\hat{\boldsymbol{u}}_\alpha^{hp}(\boldsymbol{x}) + \sum_{i=1}^{N_{\mathscr{R}}} \mathscr{H}_i(\boldsymbol{x})\tilde{\boldsymbol{u}}_{i\alpha}^{hp}(\boldsymbol{x})\right] = \sum_{\alpha=1}^{N_b} \varphi_\alpha(\boldsymbol{x})\boldsymbol{u}_\alpha^{hp}(\boldsymbol{x}) \\
&= \sum_{\alpha=1}^{N_b} \varphi_\alpha(\boldsymbol{x}) \left[\sum_{j=1}^{D_L} \underline{\hat{\boldsymbol{u}}}_{\alpha j} L_{j\alpha}(\boldsymbol{x}) + \sum_{i=1}^{N_{\mathscr{R}}} \mathscr{H}_i(\boldsymbol{x}) \sum_{j=1}^{D_L} \underline{\tilde{\boldsymbol{u}}}_{i\alpha j} L_{j\alpha}(\boldsymbol{x})\right] \\
&= \sum_{\alpha=1}^{N_b}\sum_{j=1}^{D_L} \underline{\hat{\boldsymbol{u}}}_{\alpha j}\varphi_\alpha(\boldsymbol{x})L_{j\alpha}(\boldsymbol{x}) + \sum_{\alpha=1}^{N_b}\sum_{j=1}^{D_L}\sum_{i=1}^{N_{\mathscr{R}}} \underline{\tilde{\boldsymbol{u}}}_{i\alpha j}\varphi_\alpha(\boldsymbol{x})\mathscr{H}_i(\boldsymbol{x})L_{j\alpha}(\boldsymbol{x}) \\
&= \sum_{\alpha=1}^{N_b}\sum_{j=1}^{D_L} \underline{\hat{\boldsymbol{u}}}_{\alpha j}\hat{\phi}_{j\alpha}(\boldsymbol{x}) + \sum_{\alpha=1}^{N_b}\sum_{j=1}^{D_L}\sum_{i=1}^{N_{\mathscr{R}}} \underline{\tilde{\boldsymbol{u}}}_{i\alpha j}\tilde{\phi}_{i\alpha j}(\boldsymbol{x})
\end{aligned}$$

where $\boldsymbol{u}_\alpha^{hp}$, $\alpha = 1,\ldots,N_b$, are local approximations of $\boldsymbol{u}$ defined on ω_α, $\tilde{\phi}_{i\alpha j}(\boldsymbol{x}) = \varphi_\alpha(\boldsymbol{x})\mathscr{H}_i(\boldsymbol{x})L_{j\alpha}(\boldsymbol{x})$, $\alpha = 1,\ldots,N_b$, $j = 1,\ldots,D_L$, $i = 1,\ldots,N_{\mathscr{R}}$, are generalized FE shape functions of degree p.

The generalized FE shape functions at a node $\boldsymbol{x}_\alpha$ are given by

$$\begin{aligned}\boldsymbol{\Phi}_\alpha^p &= \{\hat{\phi}_{j\alpha}\}_{j=1}^{D_L} \bigcup_{i=1}^{N_{\mathscr{R}}} \mathscr{H}_i \{\hat{\phi}_{j\alpha}\}_{j=1}^{D_L} \\ &= \varphi_\alpha \times \{1, L_{2\alpha},\ldots,L_{D_L\alpha}, \\ &\quad \mathscr{H}_1, \mathscr{H}_1 L_{2\alpha},\ldots,\mathscr{H}_1 L_{D_L\alpha}, \\ &\quad \mathscr{H}_2, \mathscr{H}_2 L_{2\alpha},\ldots,\mathscr{H}_2 L_{D_L\alpha},\ldots, \\ &\quad \mathscr{H}_{N_{\mathscr{R}}}, \mathscr{H}_{N_{\mathscr{R}}} L_{2\alpha},\ldots,\mathscr{H}_{N_{\mathscr{R}}} L_{D_L\alpha}\}\end{aligned}$$

The enrichment functions $\mathscr{H}_i(\boldsymbol{x})L_{j\alpha}(\boldsymbol{x})$, $j = 1,\ldots,D_L$, $i = 1,\ldots,N_{\mathscr{R}}$, are denoted *high-order step functions*. The numerical examples presented in Section 3 show that these functions can deliver optimal convergence rates.

Approximations of the same polynomial degree are used above for the continuous, $\hat{\boldsymbol{u}}^{hp}$, and discontinuous, $\tilde{\boldsymbol{u}}_i^{hp}$, components of the solution. However, this is not necessary. Hereafter, p and q are used to denote the polynomial degree of $\hat{\boldsymbol{u}}^{hp}$ and $\tilde{\boldsymbol{u}}_i^{hp}$, respectively. In the numerical examples analyzed in Section 3, GFEM approximations with $1 \leq p,q \leq 4$ are used. Below, we list a few examples of GFEM approximations for branched cracks..

- GFEM($p = 1, q = 1$). In this case, the local approximations $\hat{\boldsymbol{u}}_\alpha^{hp}$, $\tilde{\boldsymbol{u}}_{i\alpha}^{hp}$, $\alpha = 1,\ldots,N_b$, $i = 1,\ldots,N_{\mathscr{R}}$, are constant over ω_α, i.e., $\{L_{j\alpha}\}_{j=1}^{D_L} = \{1\}$ and the shape functions at a node $\boldsymbol{x}_\alpha$ are given by
$$\boldsymbol{\Phi}_\alpha^{p=q=1} = \varphi_\alpha \times \{1, \mathscr{H}_1, \mathscr{H}_2,\ldots,\mathscr{H}_{N_{\mathscr{R}}}\} \tag{7}$$
which are the same generalized FE shape functions presented in [6], i.e., we recover the simplest possible case, that of a piecewise linear approximation of $\boldsymbol{u}$.
- GFEM($p = 2, q = 0$). This case corresponds to the generalized FE shape functions introduced in [17, 18]. The shape functions at a node $\boldsymbol{x}_\alpha$ are given by
$$\boldsymbol{\Phi}_\alpha^{p=2,q=0} = \varphi_\alpha \times \left\{1, \frac{(x-x_\alpha)}{h_\alpha}, \frac{(y-y_\alpha)}{h_\alpha}, \frac{(z-z_\alpha)}{h_\alpha}\right\} \tag{8}$$
These shape functions, of course, can not represent the discontinuous components of the solution $\tilde{\boldsymbol{u}}_i^{hp}$. In Section 3, we use these functions in combination with meshes fitting the crack surfaces. These meshes model the crack surfaces explicitly like in the FEM.
- GFEM($p = 2, q = 2$). The shape functions at a node $\boldsymbol{x}_\alpha$ are given by
$$\begin{aligned}\boldsymbol{\Phi}_\alpha^{p=q=2} &= \varphi_\alpha \times \left\{1, \frac{(x-x_\alpha)}{h_\alpha}, \frac{(y-y_\alpha)}{h_\alpha}, \frac{(z-z_\alpha)}{h_\alpha},\right. \\ &\quad \mathscr{H}_1, \mathscr{H}_1\frac{(x-x_\alpha)}{h_\alpha}, \mathscr{H}_1\frac{(y-y_\alpha)}{h_\alpha}, \mathscr{H}_1\frac{(z-z_\alpha)}{h_\alpha}, \\ &\quad \mathscr{H}_2, \mathscr{H}_2\frac{(x-x_\alpha)}{h_\alpha}, \mathscr{H}_2\frac{(y-y_\alpha)}{h_\alpha}, \mathscr{H}_2\frac{(z-z_\alpha)}{h_\alpha},\ldots, \\ &\quad \left.\mathscr{H}_{N_{\mathscr{R}}}, \mathscr{H}_{N_{\mathscr{R}}}\frac{(x-x_\alpha)}{h_\alpha}, \mathscr{H}_{N_{\mathscr{R}}}\frac{(y-y_\alpha)}{h_\alpha}, \mathscr{H}_{N_{\mathscr{R}}}\frac{(z-z_\alpha)}{h_\alpha}\right\}\end{aligned} \tag{9}$$

- GFEM($p=2,q=1$). The shape functions at a node $\boldsymbol{x}_\alpha$ are given by

$$\boldsymbol{\Phi}_\alpha^{p=2,q=1} = \varphi_\alpha \times \left\{ 1, \frac{(x-x_\alpha)}{h_\alpha}, \frac{(y-y_\alpha)}{h_\alpha}, \frac{(z-z_\alpha)}{h_\alpha}, \mathscr{H}_1, \mathscr{H}_2, \ldots, \mathscr{H}_{N_{\mathscr{R}}} \right\} \tag{10}$$

  If we have a single (non-branching) discontinuity in the domain and the problem is two-dimensional, the shape functions are reduced to

$$\boldsymbol{\Phi}_\alpha^{p=2,q=1} = \varphi_\alpha \times \left\{ 1, \frac{(x-x_\alpha)}{h_\alpha}, \frac{(y-y_\alpha)}{h_\alpha}, \mathscr{H}_1 \right\} \tag{11}$$

  These shape functions are equivalent to those proposed by Stazi et al. [22]. In Section 3, we compare the performance of these functions with those from GFEM($p=2,q=2$).

Let us note that the high-order approximations developed above are, of course, applicable to the GFEM for polycrystals presented in [6].

Another formulation for modeling branching cracks based on the partition of unity framework was proposed by Daux et al. [19]. They proposed piecewise linear approximations to model branching cracks in two-dimensions. A detailed comparison between the two approaches can be found in [6].

2.1. Selection of nodal enrichment

In general, several step functions $\mathscr{H}_i$ are constant over the support ω_α of a given partition of unity function φ_α and should therefore not be used in actual computations. Linear dependence among the constant and step functions can also occur. A simple procedure to eliminate these linear dependences was presented in [6, Sec. 6.2]. In the case of branched cracks, the procedure is essentially the same with two exceptions: (i) Nodes in the set $\mathscr{I}_{\text{front}}$ are not enriched with discontinuous functions; (ii) In the computation of the intersection of boundary, $\partial\mathscr{R}_i$, of regions $\mathscr{R}_i$, $i=1,\ldots,N_{\mathscr{R}}$, with the support ω_α of nodes $\boldsymbol{x}_\alpha, \alpha=1,\ldots,N_b$, only the portions of $\partial\mathscr{R}_i$ that are on a crack surface are considered. The algorithm is presented in Figure 2 and illustrated in Figure 3. Figures 18 and 22 illustrate the application of this algorithm in three dimensions. In these figures, nodes with a solid sphere have continuous, $\hat{\phi}_{j\alpha}(\boldsymbol{x}) = \varphi_\alpha(\boldsymbol{x}) L_{j\alpha}(\boldsymbol{x})$, and discontinuous, $\tilde{\phi}_{i\alpha j}(\boldsymbol{x}) = \varphi_\alpha(\boldsymbol{x}) \mathscr{H}_i(\boldsymbol{x}) L_{j\alpha}(\boldsymbol{x})$, GFEM shape functions. All other nodes have continuous GFEM shape functions only.

If high-order enrichment functions are used, the resulting generalized FE shape functions $\boldsymbol{\Phi}_\alpha$, $\alpha = 1,\ldots,N_{\mathscr{R}}$, can still be linear dependent. An algorithm for handling this case is described in [18].

2.2. Crack front enrichment

The GFEM shape functions presented in Section 2 do not use near crack front expansions as enrichment functions. The stress state in the neighborhood of a crack front is not well known in three-dimensions, and analytical expansions are available only for particular crack geometries [30, 31]. Complex crack front geometries, curved crack surfaces or the intersection of the crack surface with the boundary, create complex stress distributions that are, in general, not amenable to closed form expansions. Similarly, non-linear fracture models generate stress states that are not amenable to analytical expansions in the neighborhood of a process zone.

Two additional difficulties with near crack front enrichment functions are their numerical integration and the need to enrich several layers of elements around the crack front in order to achieve optimal convergence rates [25, 27]. Integration errors may lead to wrong conclusions in a convergence analysis since they may cancel discretization errors when computing, for example, the strain energy. In this

Create geometrical representations for regions $\mathscr{R}_i,\ i=1,\ldots,N_{\mathscr{R}}$. Region $\mathscr{R}_i$ can be larger (but not smaller) than previously defined and illustrated in Figure 1. The only constraint is that $\mathscr{R}_i \cap \mathscr{R}_j$, $i \neq j$, is non-empty only along crack surfaces.
foreach *node* $\boldsymbol{x}_\alpha, \alpha = 1,\ldots,N_b$, **do**
  if $\alpha \in \mathscr{I}_{front}$ **then**
    continue;
  endif
  foreach *region* $\mathscr{R}_i,\ i=1,\ldots,N_{\mathscr{R}},\ \in \Omega_{branch}$ **do**
    if $\omega_\alpha \cap \partial\mathscr{R}_i \neq \emptyset$ **then**
      if *Intersection is along a crack surface* **then**
        Enrich node $\boldsymbol{x}_\alpha$ with step function $\mathscr{H}_i$
      endif
    endif
  endfch
  if *node* $\boldsymbol{x}_\alpha$ *has more than one step function enrichment* **then**
    Discard one of them.
  endif
  Add high-order step functions to the node if $q > 1$.
endfch

Figure 2. Algorithm to select step functions for nodes in neighborhood Ω_{branch} of a branched crack.

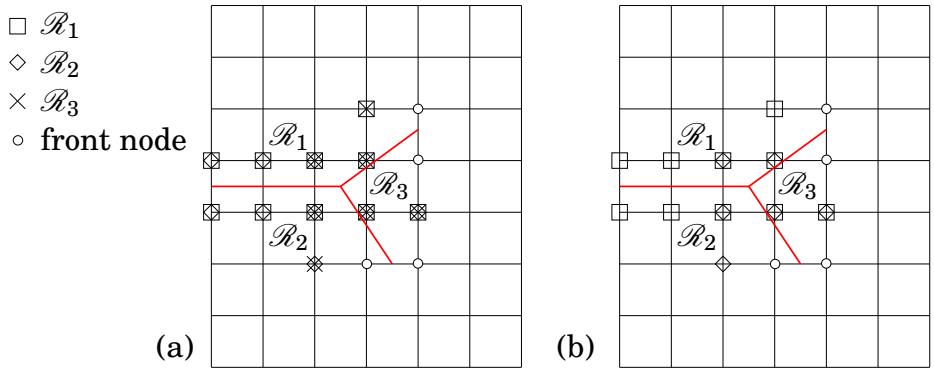

Figure 3. Nodal enrichment procedure for a branched crack in a two-dimensional domain: (a) enrichment functions are added to Ω_{branch} defined in Figure 1; and (b) surplus enrichment functions are eliminated. Note that nodes on the crack front (with index in $\mathscr{I}_{\text{front}}$) are not enriched. The procedure is detailed in the algorithm reported in Figure 2.

paper, we follow the classical FEM approach of resolving the non-smooth displacement field near a crack front by local mesh refinements combined with high-order approximations [32]. This approach avoids the difficulties and limitations related to near crack front enrichment functions while being able to deliver high convergence rates as demonstrated in Section 3. The construction of *hp* discretizations in the neighborhood of a crack front is not difficult in the generalized FEM since crack surfaces are allowed to cut elements. The mesh refinement can, therefore, be performed *as if there were no cracks in the domain*. Illustrative examples are presented in Section 3.

2.3. Equivalence of approximation spaces

In [6, Sec. 4], we have shown that the discrete spaces spanned by linear FEM shape functions and linear GFEM functions $(p=1,q=1)$ are identical when meshes fitting the crack surfaces are used. GFEM shape functions $(p=1,q=1)$ are given in (7). The same proof can be used to show the equivalence between the corresponding families of high-order GFEM shape functions. I.e., the following families of shape functions, when defined on meshes fitting the crack surfaces, are equivalent:

(i) GFEM $(p,q=0)$ with crack surfaces explicitly modeled like in the FEM. An example of shape functions from this family is given by (8). In Section 3.1.1, we use the acronym *EC* (explicit crack) to identify this family;
(ii) GFEM $(p=q)$. An example of shape functions from this family is given by (9). In Section 3.1.1, we use the acronym *BC* (boundary crack) to identify this family.

The discrete spaces spanned by these two families of functions are identical. The corresponding discretizations have the same number of degrees of freedom and the GFEM solutions computed on these discretizations are identical.

3. EXAMPLES

To assess the proposed high-order generalized FEM approximation for branched cracks, we performed a series of benchmark analyses. The quality of our results was measured using the relative error in energy norm

$$\|e\| = \frac{\sqrt{U_{exact} - U_{approx}}}{\sqrt{U_{exact}}}, \tag{12}$$

where U is the strain energy. The value of the exact strain energy, U_{exact}, was estimated using the procedure described in [33]. The estimation is based on a priori error estimates in energy norm and a sequence of GFEM solutions generated with *p*-enrichments. The approach assumes that the discretized energy converges monotonically. Using a-priori error estimates we get

$$\frac{\log \frac{U_{exact}-U_p}{U_{exact}-U_{p-1}}}{\log \frac{U_{exact}-U_{p-1}}{U_{exact}-U_{p-2}}} \approx \frac{\log \frac{N_{p-1}}{N_p}}{\log \frac{N_{p-2}}{N_{p-1}}} := Q, \tag{13}$$

where U_i are the values of the strain energy for different number of degrees of freedom N_i. The exact energy, U_{exact}, is computed by solving the non-linear equation

$$\frac{U_{exact}-U_p}{U_{exact}-U_{p-1}} \approx \left\{ \frac{U_{exact}-U_{p-1}}{U_{exact}-U_{p-2}} \right\}^Q.$$

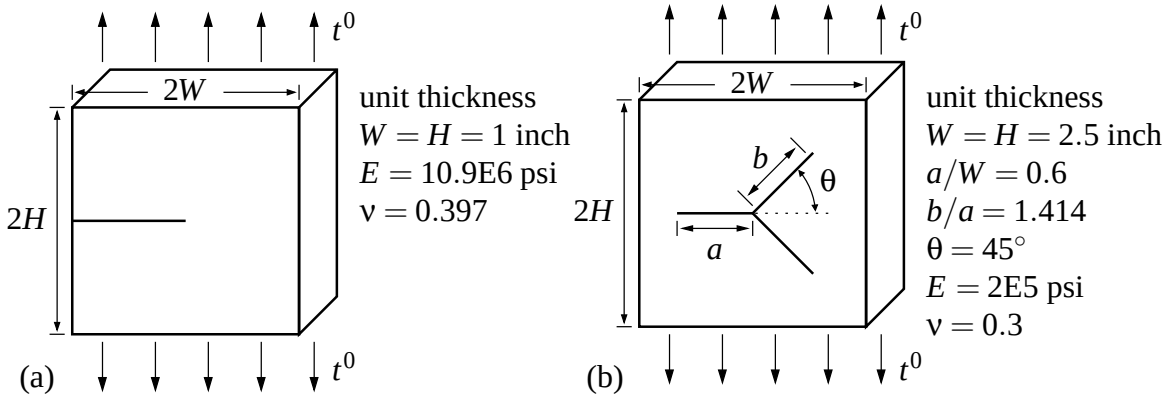

Figure 4. The benchmark tests.

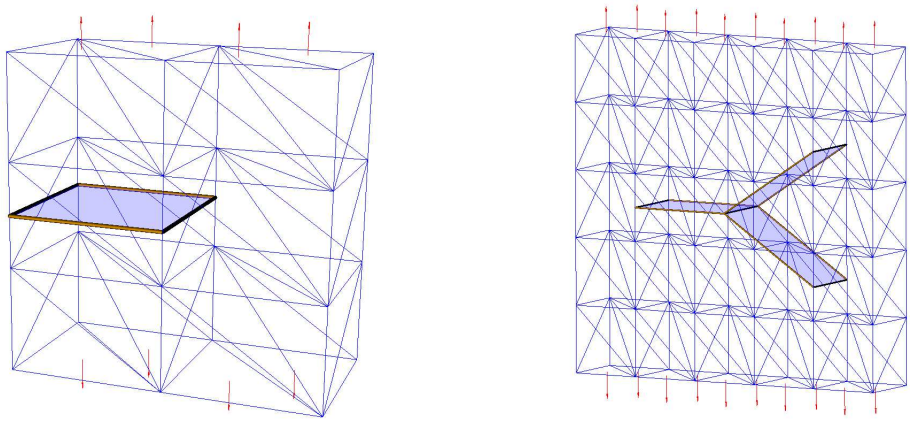

Figure 5. Examples of discretization for through-the-thickness (left) edge crack and (right) triple-joint crack.

The error and the convergence rate in energy norm for a GFEM solution can then be computed using U_{exact}.

3.1. Two benchmark tests

The benchmarks used for the convergence analyses are two three-dimensional isotropic plates with through-the-thickness edge and triple joint cracks under unit tension. Both examples are in small strain isotropic elasticity and in both cases the specimens are loaded in the vertical direction. Specimen setups and material properties are reported in Figure 4. An example of the discretizations used in this study is shown in Figure 5. As described next, we performed a series of analyses with different discretizations and refi nement strategies.

3.1.1. Edge crack For the edge crack test, we considered three families of discretizations:

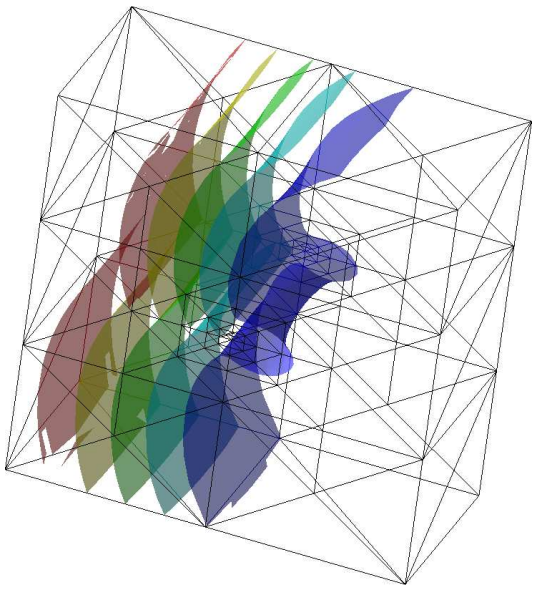

Figure 6. Edge crack: three-dimensional effect close to the crack front (isosurfaces of the norm $\|\boldsymbol{u}\|$ of the displacement field; $\|\boldsymbol{u}\|$ is not constant in the transversal direction around the crack front).

1. Meshes with an explicit crack modeled with double nodes like in the FEM. The generalized FEM shape functions used with this type of discretization are from the family GFEM$(p, q = 0)$ defined in Section 2 and introduced in [18]. The acronym *EC* (explicit crack) is used to identify a discretization of this type;
2. Meshes with crack surfaces located at element boundaries, like in the previous case, but *without* double nodes. The crack is modeled with step functions and generalized FEM shape functions from the family GFEM(p, q) are used. A discretization of this type is identified by the acronym *BC* (boundary crack). As an example, a linear continuous and discontinuous approximation of the displacement field on a mesh from this family is identified by GFEM$(p = 1, q = 1)$, *BC* or simply by $p1q1, BC$;
3. Discretizations with crack surfaces passing through the elements as shown in Figure 5. The shape functions GFEM(p, q) are also used with this family. The acronym *CC* (cutting crack) identifies a member of this family. A quadratic continuous and discontinuous approximation of the displacement field on a mesh from this family is identified by GFEM$(p = 2, q = 2)$, *CC* or simply by $p2q2, CC$.

Figure 6 shows the three-dimensional behavior of the solution near the crack front. As we have used a Poisson's ratio larger than zero, $\|\boldsymbol{u}\|$ is not constant in the transversal direction around the crack front. In the following, we assume $\lambda = 0.5$ as the order of the singularity (smoothness parameter) in the estimates for the convergence rates of the error norm reported in [33]. The smallest eigenvalue of the asymptotic expansion of the elasticity solution in the neighborhood of the crack vertices is larger than 0.5 [31]. Far from the vertices, the smallest eigenvalue is equal to 0.5, the classical two-dimensional case. The singularity of the solution far from the vertices will thus govern the convergence rate. The value of the exact strain energy for this problem, $U_{exact} = 8.171644 \times 10^{-7}$ lb.in, was estimated using

the procedure described previously.

Homogeneous *h*-refinement We first studied the effect of homogeneous *h*-refinement. In this case, the asymptotic rate of convergence in energy norm with respect to the number of degrees of freedom is given by $\beta = 1/3 \min\{p, \lambda\}$, with p the polynomial order of the approximation and λ a smoothness parameter. Since the solution is not smooth, the smoothness parameter will govern the rate of convergence which is given by $\beta = 0.5/3 \approx 0.166$.

A summary of our results is shown in Figures 7 and 8. In all cases, convergence rates in energy norm asymptotically approach the theoretical rate. There are however some differences in terms of the error produced by the various approximations. When a crack is placed along element boundaries, the curves obtained with *EC* and *BC* discretizations are indistinguishable – although the shape functions are different, both approximations span the same approximation spaces. This in agreement with the analysis presented in Section 2.3. On the other hand, the analyses with meshes cutting crack, *CC*, produced a slightly higher error when compared to the case of a crack placed along element boundaries. A-priori error estimates for the *h*-version of the generalized or standard finite element method are of the form [28, 33, 34]

$$\|u - u_h\| \leq C \frac{1}{N^\beta} \|u\|$$

Therefore, the constant C in the inequality above is larger for discretizations from the *CC* family than for the *BC* family. The GFEM shape functions from the *BC* and *CC* families are built using the same procedure. Linear and quadratic functions from these families are given by (7) and (9), respectively. The only difference between the resulting shape functions is the location of crack surfaces with respect to the support of the partition of unity functions. In the case of the *BC* family, the location coincides with boundary of elements while in the *CC* family it does not, in general. The support of a partition of unity function φ_α is the union of the finite elements sharing a vertex node x_α. A function φ_α has discontinuous first derivatives along the boundaries of the elements composing its support and continuous derivatives elsewhere. Therefore, in the case of the *BC* family, cracks "cut" φ_α along surfaces where the function has discontinuous first derivatives. This apparently may lead to a smaller constant C than when the cut is done elsewhere. Another possible reason for the difference in performance between the two families, is the location of the crack front with respect to the element boundaries. In the case of the *BC* family, crack fronts are located along element edges while in the case of the *CC* family they are, in general, located along element faces (cf. Figure 5). This argument is supported by the fact that the difference in performance between the two families tend to disappear when non-uniform meshes around the crack front are used. Local mesh refinement around the fronts tend to create element edges at or very close to the fronts and therefore reduces the difference between the two discretizations. This effect is shown in Figures 14 and 15 which are analyzed in detail later on.

A lower polynomial degree for the discontinuous components of the solution, i.e., $q < p$ instead of $q = p$, produces a consistently higher error compared to the case with $p = q$ in all the analyses. In particular, we used the interpolation scheme proposed by Stazi et al. [22] for which $p = 2$ and $q = 1$. As shown in Figure 8, although the asymptotic convergence rate is the same, the error is consistently higher when using this scheme (compare $\square$ to $\times$ or $\bigcirc$ and $*$ to $\triangle$). As a further comparison, shown in Figure 9, we note that the errors produced by Stazi et al.'s scheme and the linear interpolation scheme $p = q = 1$ are comparable for quite large range of degrees of freedom.

Non-Uniform *h*-refinement Next, we considered the effect of non-uniform *h*-refinement at the crack front. It is possible to create sequences of non-uniform meshes such that the rate of convergence

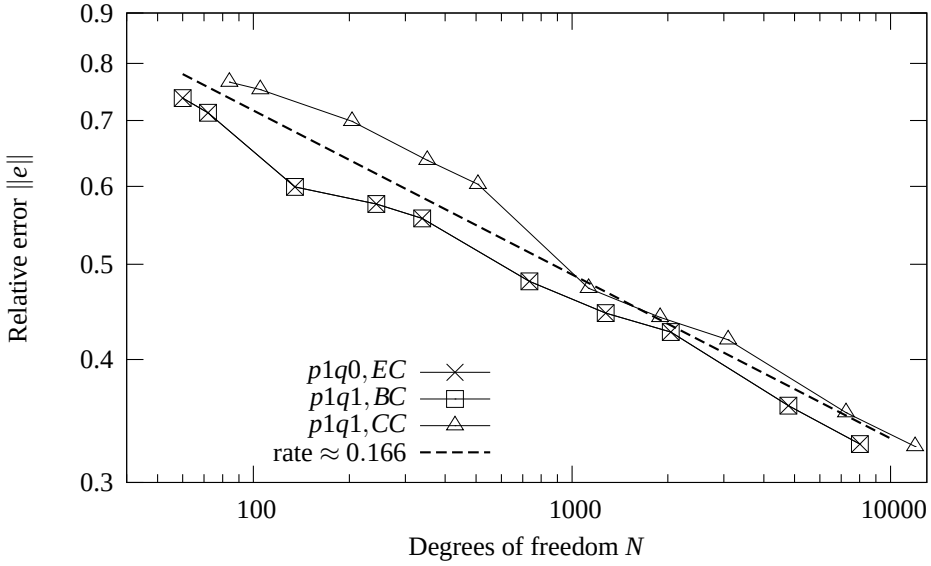

Figure 7. Edge crack: convergence rates in energy norm for homogeneous *h*-refinement of meshes from families EC with $p = 1$, $q = 0$, BC and CC with $p = q = 1$.

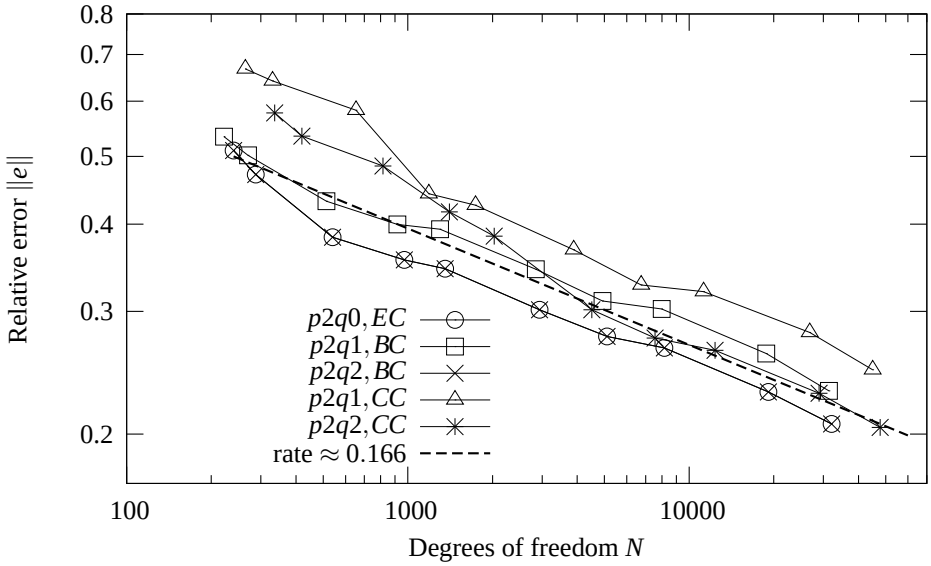

Figure 8. Edge crack: convergence rates in energy norm for homogeneous *h*-refinement of meshes from families EC with $p = 1$, $q = 0$, BC and CC with $p = q = 2$ and $p = 2$, $q = 1$.

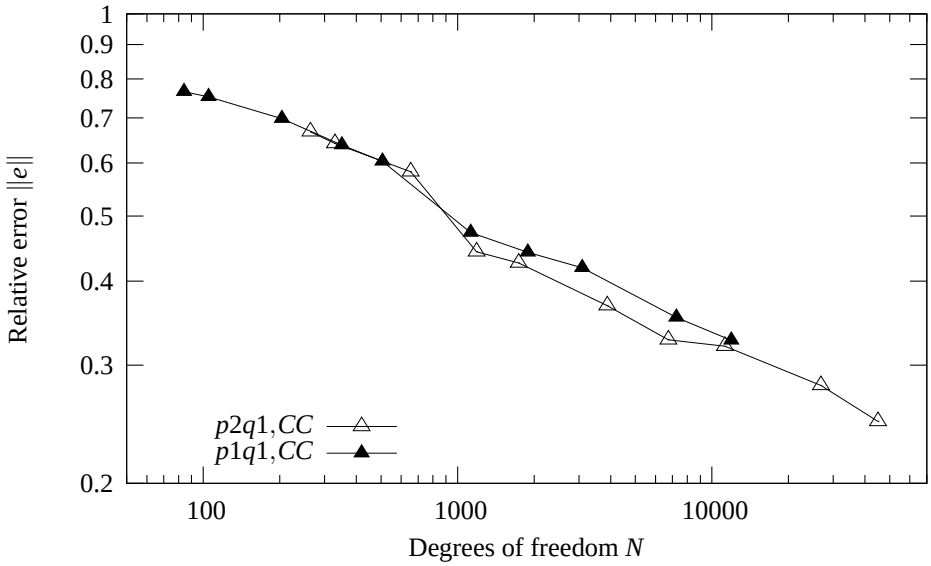

Figure 9. Edge crack: convergence rates in energy norm for homogeneous *h*-refinement of meshes from family *CC* with $p = q = 1$ and $p = 2$, $q = 1$.

is the same as that for problems with smooth solutions [33]. Therefore, in this case, the rate of convergence in energy norm is $\beta = 1/3\{p\}$ [33]. Thus, $\beta = 1/3 \approx 0.333$ for linear approximations and $\beta = 2/3 \approx 0.666$ for quadratic approximations. The construction of such a sequence of meshes, however, requires a-posteriori error indicators. In this section, we investigate an alternative approach geared towards fracture mechanics problems. Sequences of non-uniform meshes were created as follows.

(i) Create meshes locally refined around the crack front by successively bisecting all elements with the crack front at their boundary. The marked-edge algorithm [35, 36] was used to select element edges for bisection. In all discretizations, the crack fronts are located at the boundary of elements, as discussed in Section 2 and proposed in [21]. Three levels of refinement at the crack front are used in the computations: 10, 15 and 17. These refinements are denoted, hereafter, by the acronyms $F10$, $F15$ and $F17$, respectively. Figure 10 shows mesh $(CC, F15)$. Note that since the crack surface is allowed to cut the elements, the mesh refinement can be performed *as if there were no cracks in the domain*. This greatly facilitates the construction of strongly refined meshes in the neighborhood of crack fronts. In addition, the aspect ratio of the elements is not affect by the presence of the crack since their boundary do not have to fit the crack surface. This is in contrast with the classical FEM.
(ii) Apply global refinements to the non-uniform meshes created as described above.

We performed *h*-convergence analysis on sequences of non-uniform meshes from all three families (*EC*, *BC* and *CC*). The results are discussed below.

The effect of the refinement level at the crack front is shown in Figures 11 and 12. In particular, Figure 11 reports results for meshes with crack surface along element boundaries (*BC* discretizations) while Figure 12 reports results for meshes with crack cutting the elements (*CC* discretizations). Results

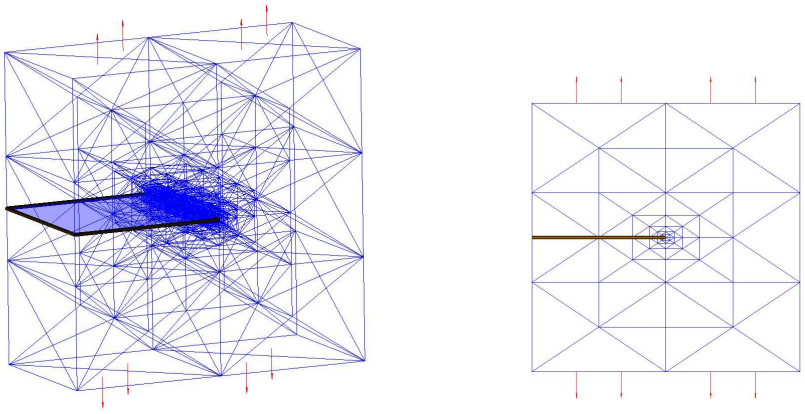

Figure 10. Mesh with strong refinement at the crack front: *CC* discretization with 15 levels of crack front refinement (mesh $CC,F15$).

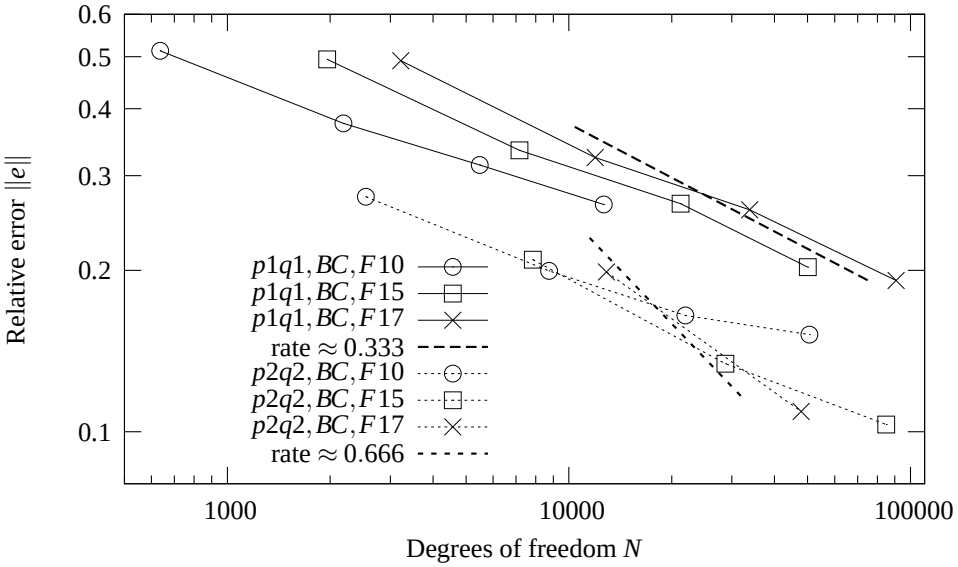

Figure 11. Edge crack: convergence rates for global *h*-refinement applied to locally refined meshes. Discretizations with crack surface along element boundaries (*BC*) and $p = q = 1$ or $p = q = 2$.

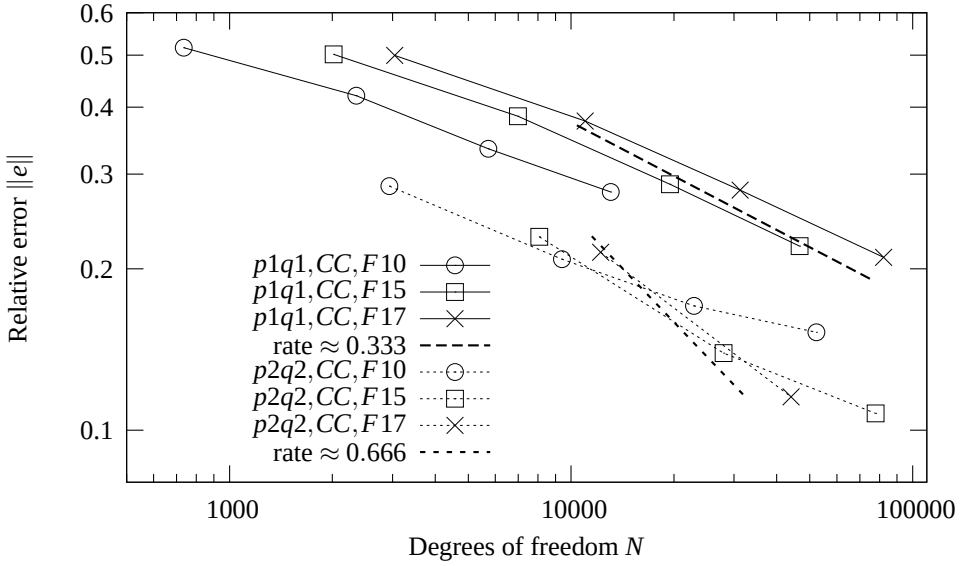

Figure 12. Edge crack: convergence rates for global *h*-refinement applied to locally refined meshes. Discretizations with crack surface cutting elements (*CC*) and $p = q = 1$ or $p = q = 2$.

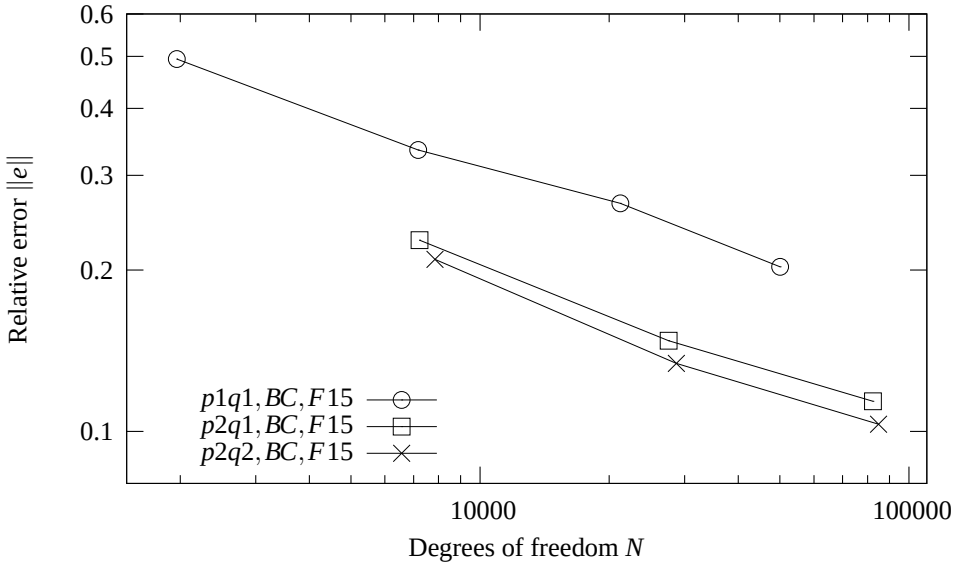

Figure 13. Edge crack: convergence rates for global *h*-refinement applied to locally refined mesh (effect of the approximation scheme).

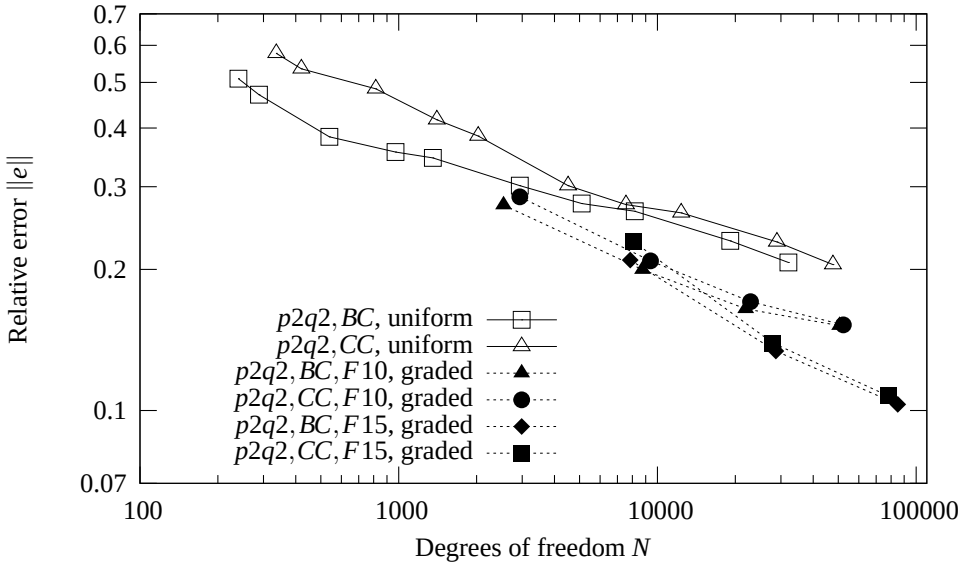

Figure 14. Edge crack: convergence rates for global *h*-refinement applied to uniform and locally refined meshes. In both cases, the *h*-refinement is applied to meshes from families *BC* and *CC* with quadratic approximation ($p = q = 2$).

for *EC* discretizations are not reported since they are the same as those for the *BC* discretizations. In all cases, global *h*-refinement is applied to locally refined meshes built as described above. It can be observed that the pre-asymptotic convergence rates increase with the refinement level at the crack front and approach those of a smooth problem. The rate of convergence for *h*-refinement applied to the discretizations $(p1q1, BC, F17)$ and $(p1q1, CC, F17)$ are 0.309 and 0.298, respectively. The ratio between these rates and those for a problem with a smooth solution are $0.309/0.333 = 0.93$ and $0.298/0.333 = 0.90$, respectively. The ratios were computed using only the last two data points in each curve. This performance is similar to that reported in [25, Sec. 4] using an approach based on enrichments with singular functions over a fixed area. The rate of convergence for *h*-refinement applied to the discretizations $(p2q2, BC, F17)$ and $(p2q2, CC, F17)$ are 0.457 and 0.483, respectively. While they are, again, smaller than the case of a problem with smooth solution, they are about 2.7 and 2.9 times, respectively, the rate of convergence for *h*-refinement applied to uniform meshes. Higher convergence rates can be obtained by further refining the mesh near the crack front. Another possibility is to use meshes in which the size of the elements decreases faster towards the singularity then in the case of the mesh shown in Figure 10 [33].

The optimal level of crack front refinement depends on the target error level. Meshes with high level of crack front refinement, $F17$ or higher, for example, are more effective for low error targets. This is shown in Figures 11 and 12, specially for the case of quadratic discretizations. This behavior is analogous to that observed in the classical finite element method [33]. The quadratic $F10$ discretizations from both *BC* and *CC* families show a significant reduction in convergence rate with global mesh refinement, indicating that the singularity along the crack front is poorly resolved by this mesh refinement level. Of course, a-posteriori error indicators [37, 38] could be used to drive the mesh refinement process instead to a-priori selecting a given level of crack front refinement as done here.

Refinement level	Double nodes, *EC*		Crack at element boundaries, *BC*			Crack cutting elements, *CC*	
	p = 1	p = 2	$p = q = 1$	$p = 2, q = 1$	$p = q = 2$	$p = q = 1$	$p = q = 2$
10	0.204	0.099	0.204	0.196	0.099	0.219	0.225
15	0.319	0.240	0.319	0.237	0.240	0.304	0.252
17	0.309	0.457	0.309	0.415	0.457	0.298	0.483
∞	0.333	0.666	0.333	0.666	0.666	0.333	0.666

Table I. Asymptotic convergence rates for *h*-refinement on locally refined meshes.

Figure 13 shows the effect of a different interpolation order for the continuous and discontinuous component of the displacement field as proposed by Stazi et al. [22]. We used meshes with the crack along element boundaries (*BC* discretizations) with 15 levels of refinement at the crack front. In this case the $p2q1$ interpolation scheme performs reasonably well when compared to the case of homogeneous *h*-refinement reported in Figure 9. We do however agree with Laborde et al. [25, Sec. 3.4.3] in stressing that the discontinuity of the displacement field along the crack surface must be represented in a sufficiently accurate way using the FEM basis as partitions of unity. This implies that the continuous and the discontinuous part of the displacement field must be compatible; in other words, they must be approximated with the same approximation space.

Figure 14 compares the performance of homogeneous *h*-refinement applied to uniform and locally refined meshes. In both cases, the *h*-refinement is applied to meshes from families *BC* and *CC* with quadratic approximation ($p = q = 2$). It can be observed that the asymptotic convergence rates for both families are very close. However, for a given number of degrees of freedom, the discretizations with cracks at element boundaries (*BC*) delivers a smaller error than the discretizations with cracks cutting the elements (*CC*). This behavior is more pronounced in the pre-asymptotic range [32] of the mesh refinement applied to uniform meshes. The difference between the *BC* and *CC* families is small in the case of locally refined meshes and essentially disappear with mesh refinement. As previously discussed, this supports the argument that the difference between the performance of two families might be due to the location of the crack front with respect to element boundaries. Figure 14 also shows that, for a given number of degrees of freedom, the graded discretizations deliver an error much smaller than those from uniform discretizations.

Table I summarizes the convergence rates in energy norm for *h*-refinement applied to non-uniform meshes from all discretizations families and different choices of approximation order. The rate of convergence for uniform *h*-refinement is only 1/6 for this problem, regardless of the order of approximation. As the table shows, locally refined meshes can deliver much higher convergence rates. Discretizations with linear approximations attain rates of convergence that are very close to those for problems with smooth solutions. Global *h*-refinements applied to non-uniform meshes $F15$ or $F17$, for example, deliver rates that are almost twice as large as those for uniform mesh refinement. We can also observe that the convergence rates for quadratic approximations increase significantly with the level of refinement around the crack front approaching those for problems with smooth solutions.

***P*-enrichment on locally refined meshes** In this section, we investigate the performance of *p*-enrichment on non-uniform meshes. Discretizations from the *CC*, *EC* and *BC* families are considered and polynomial order $1 \leq p, q \leq 4$. High-order finite element approximations on meshes that can isolate the singularity can deliver exponential convergence rates [32]. We investigate the performance of the proposed generalized FEM on meshes with 15 and 17 levels of refinement at the crack front ($F15$ and $F17$ meshes).

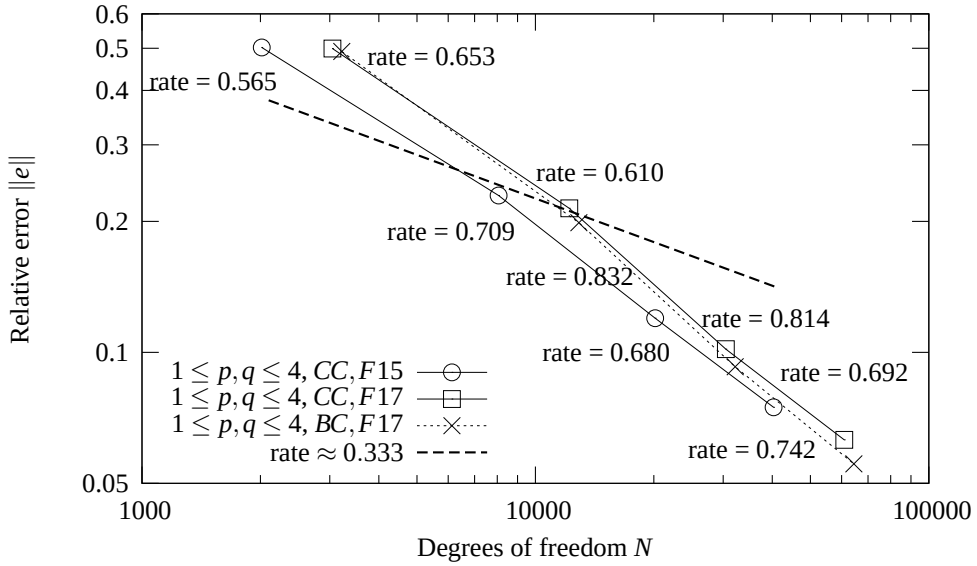

Figure 15. Edge crack: error convergence rates for *p*-enrichment on locally refined meshes (effect of the interpolation order).

The convergence rate in the energy norm for *p*-enrichment applied to *h*-uniform meshes is, for problems with non-smooth solutions and with respect to number of degrees of freedom in three dimensions, $\beta = 2/3\lambda$. For the edge crack problem, the smoothness parameter $\lambda = 0.5$ and therefore $\beta = 0.333$. *P*-enrichment applied to a locally refi ned mesh, on the other hand, can deliver much higher convergence rates, depending on how well the mesh can isolate the singularities [33].

We report only some of our results in Figure 15. We show the convergence rate for *p*-enrichment applied to meshes with cutting crack *CC* with 15 and 17 levels of crack front refi nement and for *p*-enrichment applied to *BC* discretizations (crack located at element boundaries) with 17 levels of crack front refi nement. The results for mesh with explicit cracks (*EC* discretizations) are not reported since since they are exactly the same as those for the *BC* discretizations. This, as previously discussed, is expected since *EC* and *BC* discretizations lead to the same approximation spaces. The convergence curves shown in Figure 15 have the shape of an inverted S which is typical for *p*-enrichment applied to locally refi ned meshes [33]. The convergence rates initially increases with the polynomial enrichment and later on decreases, indicating that the solution is entering the asymptotic range. All convergence rates shown in Figure 15 are in general at least twice as large as the case of *p*-enrichment applied to uniform meshes. The $F17$ meshes deliver higher convergence rates than the $F15$, as expected, since they can better isolate the singularity. However, for a given number of degrees of freedom, the $F15$ meshes give a smaller error *for the the range of polynomial orders used in the computations*. The situation might reverse for higher polynomial orders. The highest rate shown in the fi gure is $0.832/0.333 = 2.5$ times the rate for *p*-enrichment applied to uniform meshes. We can also observe that the performance of the *CC* and *BC* discretizations are very close.

A summary of all the results for the edge crack test with *CC* discretizations is reported in Figure 16. The performance of *h*-refi nement applied to uniform and locally refi ned meshes is compared with *p*-enrichment applied to locally refi ned meshes. It can be observed that the optimal strategy in terms of

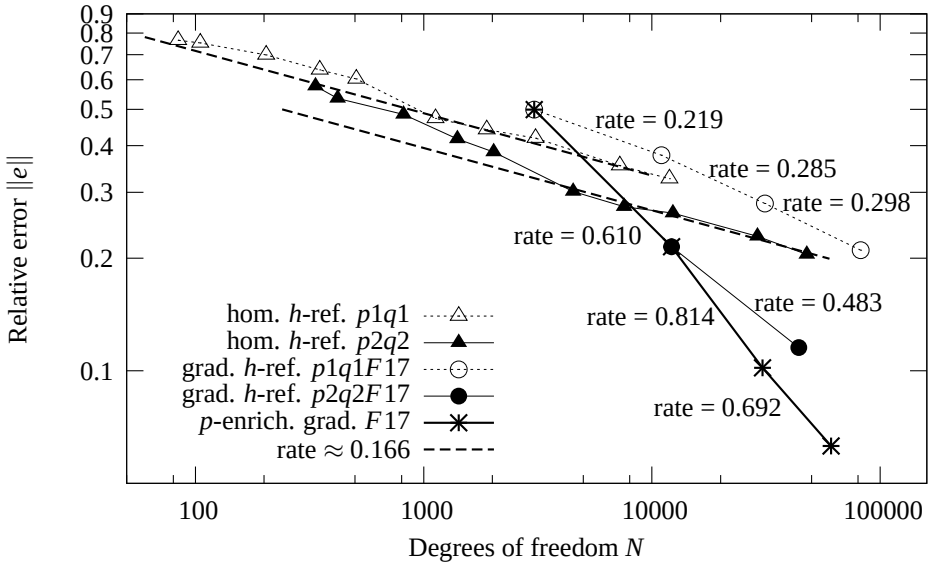

Figure 16. Edge crack: summary of convergence rates of relative energy norm error (*CC* discretizations).

error level for a given number of degrees of freedom, depends on the target error. *P*-enrichment applied to locally refined meshes is the most effective strategy for error levels below 30%. Worth noting is the improvement as the approximation order is increased from two to three on the $F17$ mesh (curve with asterisks). If this same mesh ($F17$ with $p = q = 2$) is instead globally refined and the approximation order kept constant (curve with filled circles), the improvement on the solution is less pronounced. In the first case, the rate of convergence is equal to 0.814 while in the second the rate is 0.483. The *p*-extension, in this case, delivers a smaller error using fewer degrees of freedom than the *h*-extension.

3.1.2. Triple joint crack We have performed a series of analyses on the triple joint crack problem shown in Figure 4(b). For this problem, we concentrate on *p*-extensions applied to non-uniform meshes since the edge crack problem showed that this is the most effective strategy. The same polynomial order for the continuous and discontinuous shape function is used in all computations. We also include uniform *h*-refinement results to have a baseline for comparison. The results are very similar to those reported previously for the edge crack case. In this example, we considered only discretizations in which the discontinuity surfaces cut through the finite elements as shown in Figures 5(b) and 17. The solution on elements interacting with the branched crack surface is approximated with the generalized FEM shape functions presented in Section 2. The selection of discontinuous enrichment functions at a node, if any, is done with the aid of the algorithm discussed in 2.1. Figure 18 shows nodes with discontinuous enrichment functions on uniform and non-uniform meshes. The value of the exact strain energy for this problem, $U_{exact} = 1.37178 \times 10^{-4}$ lb.in, was estimated using the procedure described previously.

Homogeneous *h*-refinements We first employed homogeneous *h*-refinements for linear ($p1q1$) and quadratic ($p2q2$) approximations. The curves corresponding to these discretizations are indicated as

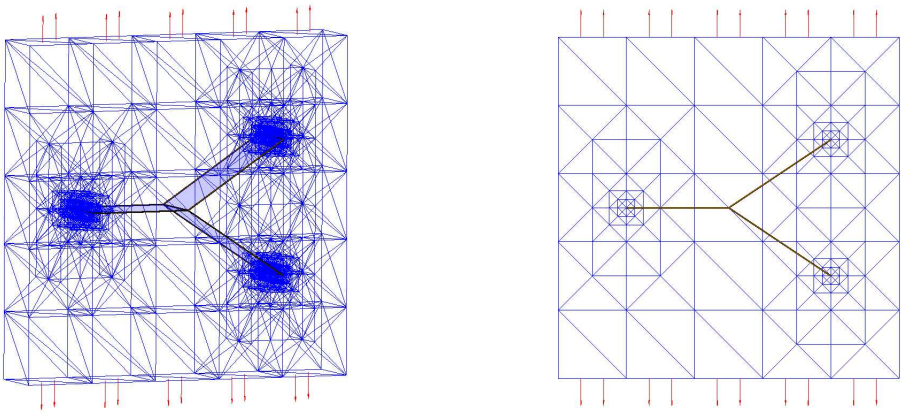

Figure 17. Mesh with strong refinement at the crack fronts: *CC* discretization with 10 levels of crack front refinement (mesh $CC, F10$).

"hom. *h*-ref $p1q1$" and "hom. *h*-ref $p2q2$" in Figure 19, respectively. The results reported in the figure show that the asymptotic convergence rate in energy norm for *h*-refinement is very close to 0.1666, like in the edge crack problem.

***P*-enrichment on locally refined meshes** The performance of *p*-enrichments on meshes locally refined at the crack fronts was also investigated. Meshes with 10 and 15 levels of refinement at the crack fronts, as shown in Figure 17, were employed. The results are shown in Figure 19 together with those for the uniform mesh refinement. We can observe that, as in the edge crack problem, strong mesh refinements at the crack fronts are able to isolate the singularities and deliver high convergence rates in the pre-asymptotic range. The reduction in convergence rate with *p*-enrichment indicates that the solution is entering the asymptotic range. This behavior is typical of *p*-extensions on locally refined meshes [32]. Stronger refinement at the crack fronts would delay this behavior. The $F15$ mesh delivers higher convergence rates than the $F10$ mesh, as expected. However, for a given number of degrees of freedom, the $F10$ mesh delivers a smaller error than the $F15$ mesh. The behavior is probably the opposite for lower error levels (note the intersection of the two curves in Figure 19). Like in the edge crack problem, we can observe that it is not practical to achieve error levels below 10% using uniform mesh refinement. *P*-extensions on locally refined meshes are quite effective for this class of problems. Figure 20 shows the von Mises stress distribution computed on the mesh with 15 levels of crack front refinement and $p = q = 3$. The presence of singularities at the crack fronts can be clearly observed.

3.2. Multi-branched crack

The flexibility and generality of the proposed approach can be appreciated by considering a more challenging problem like the one shown in Figure 21. The (21 in $\times$ 21 in $\times$ 1 in) three-dimensional plate with a multi-branched discontinuity is loaded by a unit tension. The plate material obeys linear elasticity with Young's modulus equal to 2×10^5 psi and Poisson's ratio equal to 0.3. The value of the exact strain energy, $U_{exact} = 0.382226$ lb.in, was estimated using the procedure based on a-priori error

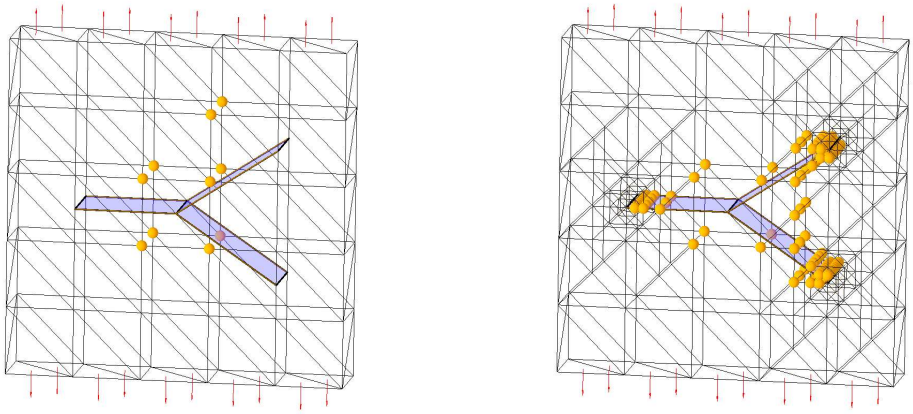

Figure 18. Nodes with a solid sphere have continuous, $\hat{\phi}_{j\alpha}(\boldsymbol{x}) = \varphi_\alpha(\boldsymbol{x})L_{j\alpha}(\boldsymbol{x})$, and discontinuous, $\tilde{\phi}_{i\alpha j}(\boldsymbol{x}) = \varphi_\alpha(\boldsymbol{x})\mathscr{H}_i(\boldsymbol{x})L_{j\alpha}(\boldsymbol{x})$, GFEM shape functions. All other nodes have continuous GFEM shape functions only. Meshes $CC, F0$ (left) and $CC, F10$ (right).

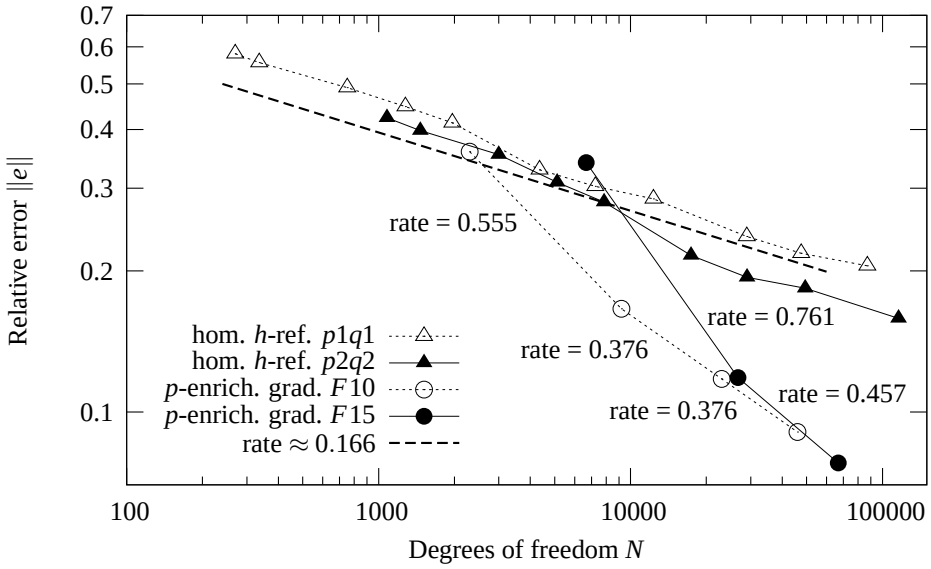

Figure 19. Triple-joint crack: summary of convergence rates of relative energy norm error (*CC* discretizations).

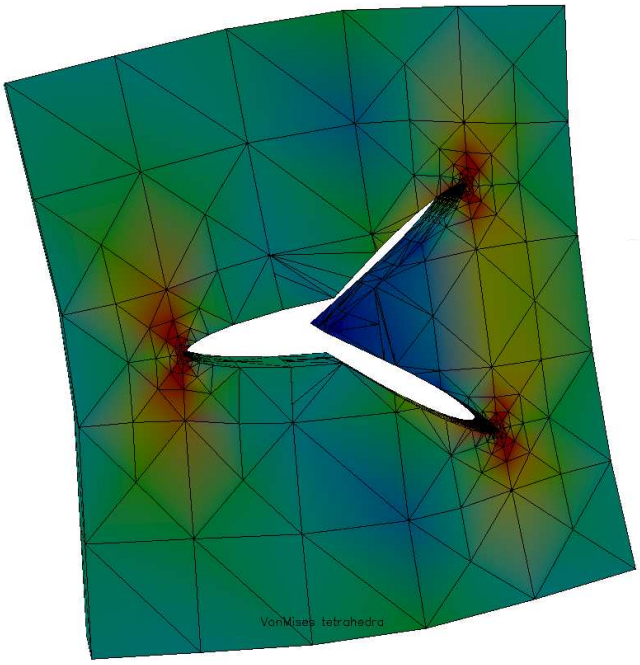

Figure 20. Von Mises stress distribution computed on mesh $CC, F15$ and $p = q = 3$.

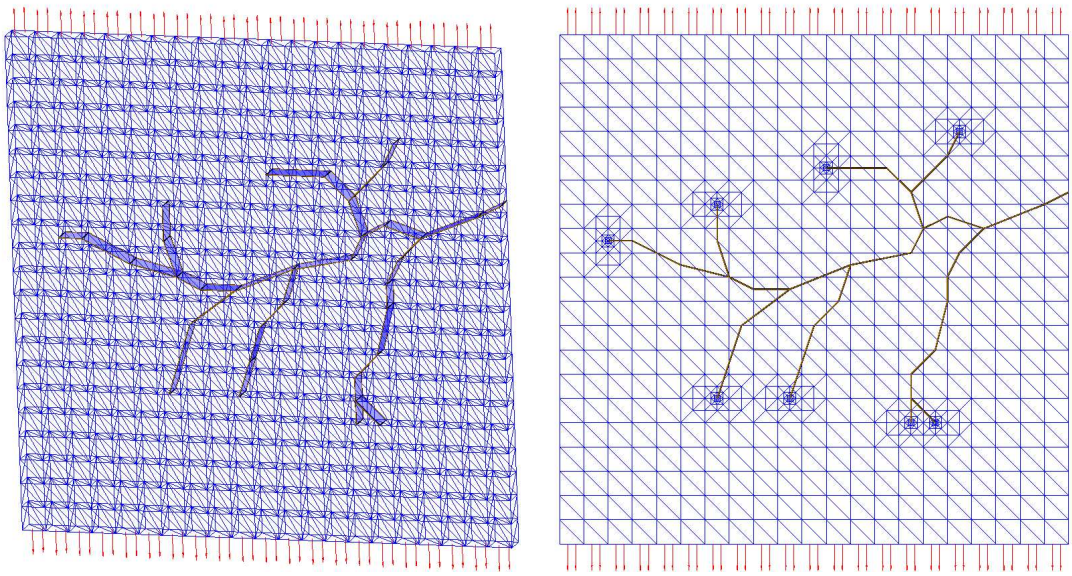

Figure 21. Multi-branched crack problem (left) with 10 levels of mesh refinement at crack fronts (right).

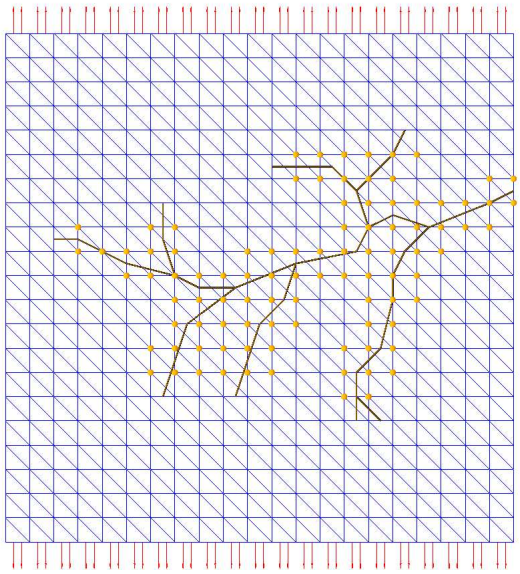

Figure 22. Nodes with a solid sphere have continuous, $\hat{\phi}_{j\alpha}(\boldsymbol{x}) = \varphi_\alpha(\boldsymbol{x})L_{j\alpha}(\boldsymbol{x})$, and discontinuous, $\tilde{\phi}_{i\alpha j}(\boldsymbol{x}) = \varphi_\alpha(\boldsymbol{x})\mathscr{H}_i(\boldsymbol{x})L_{j\alpha}(\boldsymbol{x})$, GFEM shape functions. All other nodes have continuous GFEM shape functions only. Mesh $CC,F0$.

estimates.

Like in the previous problem, we considered only discretizations from the *CC* family with 5, 10 and 15 levels of mesh refinement at the crack fronts (*CC F*5, *F*10 and *F*15 meshes). The construction of the local refinements can be done fully automatically using the location of the crack fronts. All the user needs to provide is the level of refinement used at the crack fronts. Figure 21 shows meshes *CC F*0 and *CC F*10. Figure 22 shows the nodes of mesh *CC F*0 enriched with discontinuous functions. The algorithm discussed in Section 2.1, was used to select the discontinuous enrichments functions used at each node.

Figure 23 shows the *actual* tcl [39] code used to solve the multi-branched crack problem on the discretization *CC F*10, $p = q = 3$. The code includes all steps in the analysis:

1. Loading of file with GFEM model definition. This includes nodes, elements, material and boundary conditions;
2. Loading of branched cracked geometry;
3. Local refinement of elements around each one of the seven crack fronts, i.e., the creation of mesh *CC F*10;
4. Creation of discontinuous enrichment functions based on the branched crack geometry;
5. Assignment of continuous and discontinuous enrichment functions to nodes;
6. Solution of the problem;
7. Computation of strain energy.

No user intervention is required to perform the analysis, regardless of the complexity of the branched crack surface. This allows the solution of a large number of problems and is ideal, for example, for parametric studies.

```
# read model: Nodes, elements, material, boundary conditions, etc.
readFile complexBranchedCrack.grf phfile

# create a linear analysis object
createAnalysis linear

# read branched crack definition and create a crack manager object
crackManager create crackMgID 2 crackFile "complexBranchedCrack.crf"

# Refine elements that intersect the crack fronts
set nref 10
for {set iref 0} {$iref < $nref} {incr iref} {
  crackManager refineProbMesh crackMgID 2 crackFronts
}

# create step functions and assign them to nodes
crackManager process crackMgID 2

# resulting p-order of approximation
set p 3

# Enrich nodes with continuous and discontinuous functions
enrichApprox all iso approxOrder $p

# Assemble left and right hand side
assemble

# solve linear problem
solve

# compute strain energy
work
exit
```

Figure 23. Actual tcl code used to solve the multi-branched crack problem on the discretization $CCF10$ $p = q = 3$.

***P*-enrichment on locally refined meshes** The p-version of the GFEM was used to solve this problem. Meshes with different levels of refinement at the crack fronts were used. Figure 24 reports the convergence rates in energy norm. As in the previous examples, the convergence rates increases with the level of refinement at the fronts. This indicates that the local refinements are able to isolate the singularities and extend the pre-asymptotic range of the curves. The mesh with ten levels of crack front refinement ($F10$) is the most effective for errors levels below 20%. This is similar to the triple-joint problem. For error levels below 5%, meshes with higher levels of front refinement may be more effective.

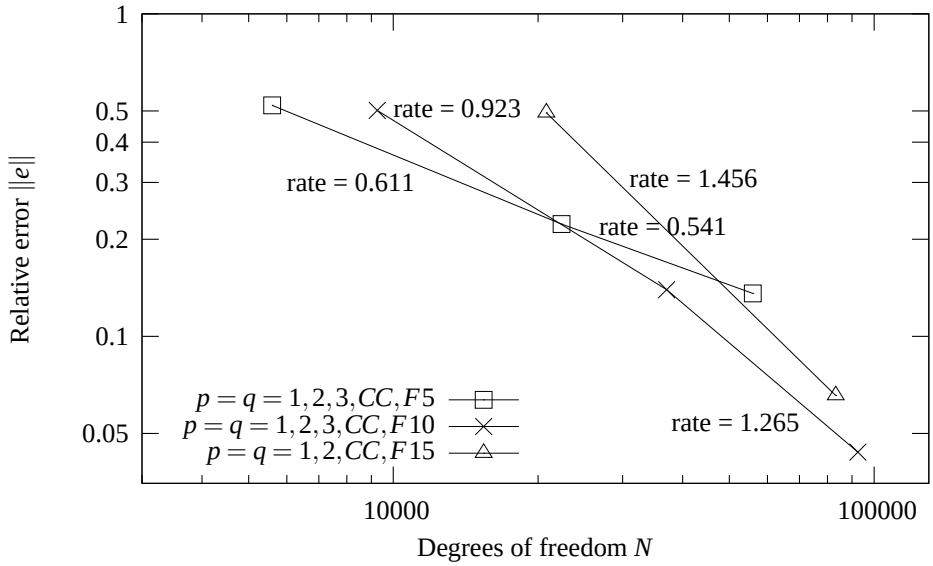

Figure 24. Multi-branched crack: *p*-enrichment on locally refined meshes.

4. SUMMARY AND CONCLUDING REMARKS

This paper presents a generalized finite element method for through-the-thickness three-dimensional branched cracks in which the crack topology is represented independently from the background finite element mesh. The method is a high-order extension to three-dimensional branched cracks of the enrichment procedure described in [6] for two-dimensional polycrystalline structures. Although the numerical examples reported in Section 3 involves through-the-thickness cracks, the formulation presented in Section 2 is valid for general three-dimensional problems. Further, cohesive or frictional contact laws [21, 40–52] can be easily incorporated by appropriate modifications of the formulation reported in [6, Sec. 5.2].

The proposed approach, based on *p*-enrichment of locally refined meshes, is geared towards simplicity and generality. Analytical expressions of near-front fields are not used. The approach is therefore suited to general linear and non-linear analyses and does not require special integration strategies for singular functions. An alternative approach for single cracks in two-dimensions was proposed by Laborde et al. [25] and Bechet et al. [27]. In their approach, singular enrichment functions are used at all finite element nodes within a prescribed distance from a crack tip. The size of the enrichment zone is kept fixed as the background mesh is refined by enriching additional nodes. This strategy is restricted to situations in which analytical expressions of near-front fields are available.

A number of important conclusions can be drawn as a result of the numerical analyses. Our findings demonstrate that crack front enrichment functions are not mandatory to achieving accurate results and high convergence rates. Instead, the combination of local refinement at crack fronts and high-order continuous and discontinuous enrichments proves to be an excellent combination which can deliver convergence rates close to that of problems with smooth solutions, specially for linear approximations (see Table I). It is worth noting here that local mesh refinement is greatly simplified since element

boundaries need not to be aligned to crack surfaces. The meshing stage is therefore truly automatic, with no need for user intervention (see Figure 23).

Another important outcome of our analyses is that the same order of approximation should be used for the continuous and discontinuous part of the displacement field – a similar remark was made by Laborde et al. [25, Sec. 3.4.3] with respect to the approximation scheme proposed by Stazi et al. [22].

As a final remark, it bears mentioning that a-posteriori error indicators [37, 38] could be used to drive the mesh refinement process instead to a-priori selecting a given level of crack front refinement as done in this work.

ACKNOWLEDGMENTS

The support of the University of Illinois to C.A. Duarte and L.G. Reno is gratefully acknowledged.

REFERENCES

[1] Archer MD, McKim RJ. Unusual stress-corrosion cracks observed in glassy Fe-40Ni-14P-6B alloy. *Journal of Materials Science* 1983; **18**(4):1125–1135.

[2] Woodtli J, Kieselbach R. Damage due to hydrogen embrittlement and stress corrosion cracking. *Engineering Failure Analysis* 2000; **7**(6):427–450.

[3] Kadono T, Arakawa M. Crack propagation in thin glass plates caused by high velocity impact. *Physical Review E* 2002; **65**(3):035107.

[4] Sharon E, Fineberg J. Microbranching instability and the dynamic fracture of brittle materials. *Physical Review B* 1996; **54**(10):7128–7139.

[5] Ravi-Chandar K, Knauss WG. An experimental investigation into dynamic fracture: II. Microstructural aspects. *International Journal of Fracture* 1984; **26**(1):65–80.

[6] Simone A, Duarte CA, Van der Giessen E. A Generalized Finite Element Method for polycrystals with discontinuous grain boundaries. *International Journal for Numerical Methods in Engineering* 2006; **67**(8):1122–1145.

[7] Saouma VE, Zatz IJ. An automated finite element procedure for fatigue crack propagation analyses. *Engineering Fracture Mechanics* 1984; **20**(2):321–333.

[8] Baehmann PL, Shephard MS. Adaptive multiple-level *h*-refinement in automated finite element analyses. *Engineering with Computers* 1989; **5**(3–4):235–247.

[9] Zavattieri PD, Dari EA, Buscaglia GC. Optimization strategies in unstructured mesh generation. *International Journal for Numerical Methods in Engineering* 1996; **39**:2055–2071.

[10] Freitag LA, Ollivier-Gooch C. Tetrahedral mesh improvement using swapping and smoothing. *International Journal for Numerical Methods in Engineering* 1997; **40**:3979–4002.

[11] Borouchaki H, George PL. Aspects of 2-d Delaunay mesh generation. *International Journal for Numerical Methods in Engineering* 1997; **40**:1957–1975.

[12] Weyer S, Fröhlich A, Riesch-Oppermann H, Cizelj L, Kovac M. Automatic finite element meshing of planar Voronoi tessellations. *Engineering Fracture Mechanics* 2002; **69**:945–958.

[13] Cavalcante-Neto JB, Martha LF, Wawrzynek PA, Ingraffea AR. A back-tracking procedure for optimization of simplex meshes. *Communications in Numerical Methods in Engineering* 2005; **21**(12):711–722.

[14] Mediavilla J, Peerlings RHJ, Geers MGD. A robust and consistent remeshing-transfer operator for ductile fracture simulations. *Computers and Structures* 2006; **84**(8–9):604–623.

[15] Chew LP. Constrained delaunay triangulations. *Algorithmica* 1989; **4**(1):97–108.

[16] Taylor RL, Zienkiewicz OC, Oñate E. A hierarchical finite element method based on the partition of unity. *Computer Methods in Applied Mechanics and Engineering* 1998; **152**(1–2):73–84.

[17] Oden JT, Duarte CA, Zienkiewicz OC. A new cloud-based *hp* finite element method. *Computer Methods in Applied Mechanics and Engineering* 1998; **153**:117–126.

[18] Duarte CA, Babuška I, Oden JT. Generalized finite element methods for three dimensional structural mechanics problems. *Computers and Structures* 2000; **77**:215–232.

[19] Daux C, Moës N, Dolbow J, Sukumar N, Belytschko T. Arbitrary branched and intersecting cracks with the extended finite element method. *International Journal for Numerical Methods in Engineering* 2000; **48**:1741–1760.

[20] Moës N, Dolbow J, Belytschko T. A finite element method for crack growth without remeshing. *International Journal for Numerical Methods in Engineering* 1999; **46**(1):131–150.

[21] Wells GN, Sluys LJ. A new method for modeling cohesive cracks using finite elements. *International Journal for Numerical Methods in Engineering* 2001; **50**:2667–2682.

[22] Stazi FL, Budyn E, Chessa J, Belytschko T. An extended finite element method with higher-order elements for curved cracks. *Computational Mechanics* 2003; **31**:38–48.

[23] Chessa J, Wang H, Belytschko T. On the construction of blending elements for local partition of unity enriched finite elements. *International Journal for Numerical Methods in Engineering* 2003; **57**:1015–1038.

[24] Mariani S, Perego U. Extended finite element method for quasi-brittle fracture. *International Journal for Numerical Methods in Engineering* 2003; **58**(1):103–126.

[25] Laborde P, Pommier J, Renard Y, Salaün M. High-order extended finite element method for cracked domains. *International Journal for Numerical Methods in Engineering* 2005; **64**:354–381.

[26] Duarte CA, Babuška I. Mesh-independent directional *p*-enrichment using the generalized finite element method. *International Journal for Numerical Methods in Engineering* 2002; **55**(12):1477–1492.

[27] Béchet E, Minnebo H, Moës N, Burgardt B. Improved implementation and robustness study of the X-FEM for stress analysis around cracks. *International Journal for Numerical Methods in Engineering* 2005; **64**:1033–1056.

[28] Melenk JM, Babuška I. The partition of unity finite element method: Basic theory and applications. *Computer Methods in Applied Mechanics and Engineering* 1996; **139**:289–314.

[29] Strouboulis T, Babuška I, Copps K. The design and analysis of the generalized finite element mehtod. *Computer Methods in Applied Mechanics and Engineering* 2000; **81**(1–3):43–69.

[30] Broberg KB. *Cracks and Fracture*. Academic Press, San Diego, 1999.

[31] Mittelstedt C, Becker W. Semi-analytical computation of 3D stress singularities in linear elasticity. *Communications in Numerical Methods in Engineering* 2005; **21**:247–257.

[32] Szabó BA. Mesh design for the *p*-version of the finite element method. *Computer Methods in Applied Mechanics and Engineering* 1986; **55**:181–197.

[33] Szabó BA, Babuška I. *Finite Element Analysis*. John Wiley & Sons, New York, 1991.

[34] Babuška I, Melenk JM. The partition of unity finite element method. *International Journal for Numerical Methods in Engineering* 1997; **40**:727–758.

[35] Bänsch E. Local mesh refinement in 2 and 3 dimensions. *Impact of Computing in Science and Engineering* 1991; **3**(2):181–191.

[36] Arnold DN, Mukherjee A, Pouly L. Locally adapted tetrahedral meshes using bisection. *SIAM Journal of Scientific Computing* 2000; **22**(2):431–448.

[37] Ainsworth M, Oden JT. A posteriori error estimation in finite element analysis. *Computer Methods in Applied Mechanics and Engineering* 1997; **142**(1):1–88.

[38] Babuška I, Strouboulis T. *The Finite Element Method and its Reliability*. Numerical Mathematics and Scientific Computation. Oxford Science Publications, New York, USA, 2001.

[39] Tool command language. `http://www.scripts.com/software/tcltk`.

[40] Xu XP, Needleman A. Numerical simulations of fast crack growth in brittle solids. *Journal of the Mechanics and Physics of Solids* 1994; **42**(9):1397–1434.

[41] Bažant ZP, Li YN. Cohesive crack with rate-dependent opening and viscoelasticity: I. Mathematical model and scaling. *International Journal of Fracture* 1997; **86**(3):247–265.

[42] Bolzon G, Corigliano A. A discrete formulation for elastic solids with damaging interfaces. *Computer Methods in Applied Mechanics and Engineering* 1997; **140**(3–4):329–359.

[43] Zhang Z, Paulino GH. Cohesive zone modeling of dynamic failure in homogeneous and functionally graded materials. *International Journal of Plasticity* 2005; **21**:1195–1254.

[44] Ortiz M, Pandolfi A. Finite-deformation irreversible cohesive elements for three-dimensional crack-propagation analysis. *International Journal for Numerical Methods in Engineering* 1999; **44**(9):1267–1282.

[45] McDevitt TW, Laursen TA. A mortar-finite element formulation for frictional contact problems. *International Journal for Numerical Methods in Engineering* 2000; **48**(10):1525–1547.

[46] Tijssens MGA, Van der Giessen E, Sluys LJ. Modeling of crazing using a cohesive surface methodology. *Mechanics of Materials* 2000; **32**:19–35.

[47] Dolbow J, Moës N, Belytschko T. An extended finite element method for modeling crack growth with frictional contact. *Computer Methods in Applied Mechanics and Engineering* 2001; **190**:6825–6846.

[48] Moës N, Belytschko T. Extended finite element method for cohesive crack growth. *Engineering Fracture Mechanics* 2002; **69**:813–833.

[49] Elices M, Guinea GV, Gómez J, Planas J. The cohesive zone model: Advantages, limitations and challenges. *Engineering Fracture Mechanics* 2002; **69**:137–163.

[50] de Borst R. Numerical aspects of cohesive-zone models. *Engineering Fracture Mechanics* 2003; **70**(14):1743–1757.

[51] Planas J, Elices M, Guinea GV, Gómez FJ, Cendón DA, I, Arbilla. Generalizations and specializations of cohesive crack models. *Engineering Fracture Mechanics* 2003; **70**(14):1759–1776.

[52] Kim TY, Dolbow J, Laursen T. A mortared finite element method for frictional contact on arbitrary interfaces. *Computational Mechanics* 2006; URL `http://dx.doi.org/10.1007/s00466-005-0019-4`. Article in press.